

Control-oriented low-speed dynamic modeling and trade-off analysis of air-breathing aerospace vehicles*

Hai-dong SHEN^{†1}, Rui CAO², Yan-bin LIU^{†‡1,3}, Fei-teng JIN², Yu-ping LU²

¹College of Astronautics, Nanjing University of Aeronautics and Astronautics, Nanjing 210016, China

²College of Automation Engineering, Nanjing University of Aeronautics and Astronautics, Nanjing 210016, China

³State Key Laboratory of Virtual Reality Technology and Systems, Beihang University, Beijing 100191, China

[†]E-mail: shenhaidong@nuaa.edu.cn; liuyb@nuaa.edu.cn

Received Aug. 1, 2019; Revision accepted Oct. 23, 2019; Crosschecked Nov. 5, 2019

Abstract: We present a control-oriented low-speed dynamic modeling and trade-off study framework for a conceptual air-breathing horizontal take-off and horizontal landing (HTHL) aerospace vehicle, which is powered by a turbine-based combined cycle engine. First, the 3D class/shape transformation method is modified to enhance the continuity property between different blocks, combined with the power function. Then, the panel method based on potential theory is employed to calculate the pressure distribution over discretized panel surfaces, resulting in the aerospace vehicle's aerodynamic coefficients. To overcome the intractability of the physics-based model, stepwise regression analysis is adopted and simplified polynomials of aerodynamic coefficients are evaluated. Finally, stability and control analysis is conducted, aiming to find the proper center-of-gravity locations under different constraints. The proposed framework is verified through a conceptual aerospace vehicle simulation, with emphasis on horizontal take-off rotation and landing nose hold-off capabilities. Simulation results indicate that the proposed framework is capable of rapid control-oriented dynamic modeling and iterative design of HTHL aerospace vehicles.

Key words: Control-oriented modeling; Horizontal take-off and horizontal landing (HTHL); Stability and control analysis; Trade-off study

<https://doi.org/10.1631/jzus.A1900366>


CLC number: V249.1

1 Introduction

Due to the low cost, high reliability, and huge flexibility, reusable air-breathing horizontal take-off and horizontal landing (HTHL) aerospace vehicles have great prospects in both civil and military applications, such as space launch, civil transport, and

military surveillance. Several projects have been put forward since the 1960s (Moses et al., 1999), but canceled due to intricate technical challenges at that time. However, since the successful flight test of X-43A in 2004, advances in integrated design methods, high-speed propulsion, and structures have further contributed to the readiness for design of such vehicles. Some new air-breathing HTHL vehicle concepts have been put forward. These can be categorized into high-speed transport aircraft (Longo et al., 2009; Roncioni et al., 2015; Piscitelli et al., 2017) and space transport vehicles (Kokan et al., 2004; Tsuchiya and Mori, 2005; Hellman et al., 2016). Corresponding research has been revitalized, focusing mainly on mission feasibility analysis (Bradford et al., 2004; Mehta et al., 2016; Zhou et al., 2017).

[‡] Corresponding author

* Project supported by the National Natural Science Foundation of China (No. 11572149), the Nanjing University of Aeronautics and Astronautics PhD Short-term Visiting Scholar Project (No. 180912DF15), the Funding of Jiangsu Innovation Program for Graduate Education, China (No. KYLX15_0318), the Fundamental Research Funds for the Central Universities of China, and the Open Funding Project of State Key Laboratory of Virtual Reality Technology and Systems, China (No. VRLAB2018C04)
 ORCID: Hai-dong SHEN, <https://orcid.org/0000-0002-2489-7225>

© Zhejiang University and Springer-Verlag GmbH Germany, part of Springer Nature 2019

To achieve HTHL capability, different combined cycle engines have been investigated, including three main types: (1) turbine-based combined cycle (TBCC) engines (Walker et al., 2009); (2) rocket-based combined cycle (RBCC) engines (Zhang et al., 2019); (3) air-augmented rocket air turbo-rocket engines (Fernández-Villacé et al., 2014). Among them, TBCC is regarded as the most promising propulsion concept in the near term due to its high specific impulse performance. In general, the TBCC engine works in the turbine mode from take-off, and the ramjet takes over at about Mach 3. Then the vehicle is accelerated to hypersonic speeds powered by dual-mode ramjet/scramjet (DMRS).

Within the flight envelope, aerodynamic and propulsion performance of aerospace vehicles changes significantly, resulting in distinct dynamic properties and handling qualities. To adequately perform the mission objectives and simultaneously ensure flight safety, it is necessary to well understand their flying qualities and controllability characteristics. However, most existing concepts remain at the mission concept stage, which focuses on operation and cost analysis, without considering flying quality. Up to now, there is no open-access control-oriented dynamic model in the literature. This encourages the development of our own integrated conceptual aerospace vehicle design and analysis tool.

Dynamic modeling of HTHL aerospace vehicles is difficult because it features complex interactions between numerous aspects, including aerodynamics, structure, propulsion, trajectory, and control. The major challenge arises from the airframe-propulsion integrated geometry generation, as the concept must satisfy the requirements in the whole flight regime. Thus, to capture the complex interactions and obtain an optimal design, the multidisciplinary design optimization (MDO) technique should be applied (Sziroczak and Smith, 2016).

Methods such as computer-aided design (CAD) and computational fluid dynamics (CFD) (Zhao et al., 2019) are widely used in detailed design. However, it is difficult to embed those into an MDO process, because of their expensive computational cost (Bowcutt, 2003). The parametric approach has been widely used in new conceptual vehicle design (Zhang et al., 2016b), as it describes the geometry numerically, and allows flexible global and local changes by modifying some main control parameters

(Zhang et al., 2018).

In the preliminary design phase, some degree of approximation is acceptable in the interest of less time and budget expenditure. Therefore, numerical engineering methods were adopted in (Jazra and Smart, 2009). The preliminary aerodynamic analysis method is based on the potential theory at subsonic/supersonic speeds and Newtonian impact theory at supersonic/hypersonic conditions (Anderson, 2010). In (Erickson, 1990), the basic idea of the panel method was introduced and the comparison between existing low-speed 3D panel codes was made. In (Zhang et al., 2016a), the inviscid modified Newton theory and Prandtl-Meyer equation were used to estimate the aerodynamic properties of a hypersonic gliding vehicle. A fast aerodynamics analysis tool (FAAT) software based on the modified Newtonian, tangent-cone, and shock/expansion methods was developed in (Lobbia, 2017), and the accuracy of this tool was validated by comparing the published wind-tunnel data of NASA HL-20 lifting-body with numerical results at Mach numbers ranging from 1.2 to 10.

For parallel TBCC engines (i.e. the turbine channel locates above the stamping channel and the two channels are set parallel) (McDaniel et al., 2009), performance characteristics under different flight conditions vary significantly (Liao et al., 2018). Thus, it is necessary to build an appropriate model. In (Spath and Moses, 1993), a 1D TBCC simulation model (TBCC-X) was published by NASA Lewis Research Center. To investigate the mode transition from Ma 2.5 to Ma 4.0, the high Mach transient engine combined cycle (HiTECC) code was developed by Stueber et al. (2010). Recently, a mathematical model was built on the Simulink platform for TBCC engine control law design in (Ma et al., 2018).

During the conceptual design phase, it is important to recognize the trade-off between good open-loop stability & control (S&C) properties and performance. This advocates for early integration of S&C into the design process. Unfortunately, most of the above-mentioned codes are proprietary and detailed information about the implementation of the pre-processing steps and input formats remain unpublished, which motivates our research. Different from our previous work on dual-mode scramjet-powered hypersonic vehicle dynamic modeling (Chen et al., 2017; Shen et al., 2018), an extension has been made

in this work, with the emphasis on low-speed dynamic modeling and center-of-gravity (CG) trade-off analysis, to ensure the HTHL ability of aerospace vehicles.

To achieve rapid dynamic modeling and interactive design, an integrated control-oriented conceptual aerospace vehicle design tool is developed in the MATLAB environment. The trade-off between high precision and efficient computing can be realized. The whole framework consists of the following main modules: (1) parametric geometry modeling; (2) aerodynamic estimation; (3) propulsion performance calculation; (4) control-relevant trade-off analysis. Good scalability is guaranteed because of its modular architecture. Other modules, like trajectory optimization and high fidelity data confusions, can be extended easily.

2 Integrated dynamic modeling

The proposed control-oriented dynamic modeling framework consists of four main parts, i.e. 3D parametric geometry modeling, panel-method based aerodynamic modeling, quasi-1D propulsion modeling, and S&C analysis (Fig. 1).

2.1 Geometry module

The geometric classes differ in a complex aerospace vehicle configuration, and thus the uniform parametric method is inadequate for modeling the entire configuration. In this study, the object configuration is divided into six components, which are forebody, midbody, aft body, wing, vertical tail, and engine cowl. Each component is constructed based on the lofting technique along the outer mold lines (OML). Then different components are moved/rotated to a specific point to assemble the whole configuration. Because of the aerospace vehicle's unique airframe integrated propulsion layout, the design of the forebody and aft body affects not only aerodynamic forces but also engine performance. Thus, the shape of the whole bottom side of the fuselage has to be designed to achieve a trade-off between propulsion and aerodynamic performance.

2.1.1 Cross-section definition

Suppose the characteristic direction is x . Then the cross-section refers to the projection onto the y - z

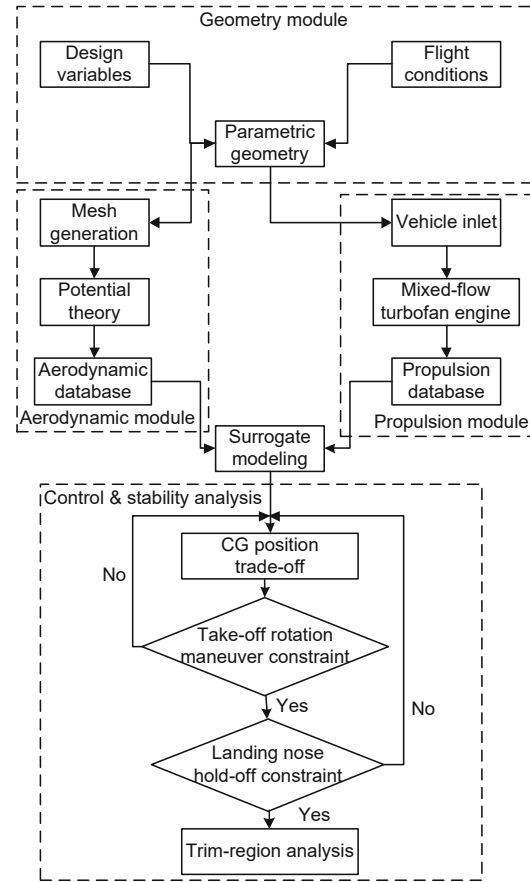


Fig. 1 Control-oriented dynamic modeling and S&C analysis framework

plane and the OML refers to the projections onto the x - y and x - z planes.

The cross-section definition is based on the class-shape transformation (CST) technique, first proposed by Kulfan (2008), in which some refinements have been made.

$$\begin{aligned}\xi(\eta) &= C_{N_2}^{N_1}(\eta)S(\eta) \\ &= 2^{-(N_1+N_2)}(\eta+0.5)^{N_1}(0.5-\eta)^{N_2}S(\eta),\end{aligned}\quad (1)$$

where $\eta \in [-0.5, 0.5]$ is the non-dimensional Y coordinate, ξ is the non-dimensional Z coordinate, C is the class function, S is the shape function, and exponents N_1 and N_2 result in different types of curves.

For x - z plane symmetry components (i.e. fuselage, nacelle, and ramps), $S(\eta) = 1$ (Figs. 2a and 2b); for wings, the coefficients of Bernstein's polynomials $S(\eta) = \sum_{i=0}^{n_0} b_i B_n^i(\eta)$ (here, B is the primary function of Bernstein's polynomials, b_i the coefficient, and n_0 the order of Bernstein's polynomials) are specified through the least square method given the object airfoil (Fig. 2c).

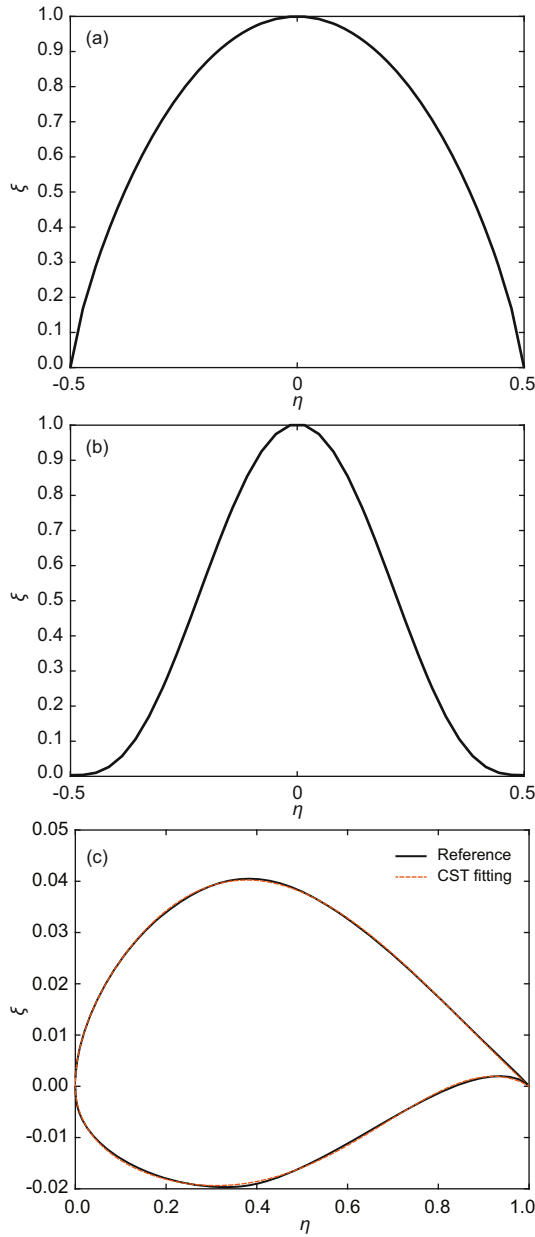


Fig. 2 Cross-section: (a) $N_1 = N_2 = 0.8$; (b) $N_1 = N_2 = 3.2$; (c) NACA64-206

2.1.2 OML definition

The OML of different components can be represented with the 2D CST method or other polynomials.

For the fuselage class components (Fig. 3), the power function is employed to describe the ridgeline. The main variables of the OML include length L , width W , and height H .

$$y = Ax^n, \quad (2)$$

where the coefficient A is a scale factor, and n is the

curvature parameter which differs for each surface.

Likewise, the planform of the trapezoidal wing can be defined by the root chord c_r , the tip chord c_t , the leading-edge sweep angle Λ_0 , and the half-span of the wing b (Fig. 4). In particular, a non-dimensional variable representing the ratio of the full span elevon area (shaded area in Fig. 4) as compared to the initial full wing surface area is introduced:

$$\eta = \frac{S_{\text{elevon}}}{S_r} = \frac{c_{\text{elevon}}}{c_r}, \quad (3)$$

where S_r is the wing area, S_{elevon} is the elevon area, and c_{elevon} is the elevon chord.

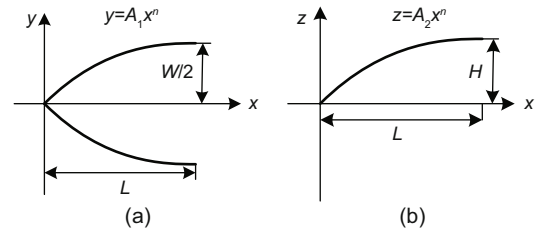


Fig. 3 Power functions: (a) L_W ; (b) L_H

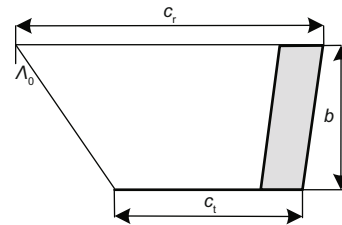


Fig. 4 Wing planform definition

It is then clear that the elevon area will be scaled along with η , wherein $\eta = 1$ corresponds to a full elevon layout and $\eta = 0$ corresponds to the lack of any control surface on the vehicle wing. The elevon area is chosen as a figure of merit to be minimized, as oversized control surfaces will result in a great expense of weight, drag, and cost. However, this aspect is out of scope for this study. The initial elevon layout is modeled as the aft 20% of the main wing chord covering the full span.

During the OML definition, additional G_0 and G_1 (coordinate and derivative) continuities have been taken into account. Ensuring smooth connecting between adjacent surfaces is a primary issue arising from component assembly (Liu et al., 2016).

2.2 Aerodynamics module

The basic idea of the panel method (PM) is to divide the vehicle surface into N surface panels and estimate the aerodynamic characteristics of complex arbitrary 3D bodies based on the superposition method.

That is

$$\begin{cases} C_p = -\frac{1}{S_{\text{ref}}} \sum_{i=1}^N c_{p,i} \Delta S_i \mathbf{n}_i, \\ C_m = -\frac{1}{S_c} \sum_{i=1}^N c_{p,i} \Delta S_i (\mathbf{n}_i \times \mathbf{r}_i), \end{cases} \quad (4)$$

where C_p and C_m represent the aerodynamic force and moment coefficients, respectively, $c_{p,i}$ is the pressure coefficient on each panel, S_{ref} is the reference area, S_c is the mean aerodynamic chord, ΔS_i is the panel area, \mathbf{r}_i is the panel radius vector, and \mathbf{n}_i is the unit out-normal vector.

2.2.1 Structured mesh generation

In this study, the structured meshes of the different components are generated automatically after parametric geometry modeling, with the desired grid density. Then, potential theory is employed to obtain panel pressure coefficients in the low-speed flight regime.

As shown in Fig. 5, for each subsurface with nodes (x_i, y_i, z_i) , $i = 1, 2, 3, 4$, the quadrilateral panel is defined with the following parameters:

1. Unit out-normal vector

$$\mathbf{n} = \frac{\mathbf{T}_1 \times \mathbf{T}_2}{|\mathbf{T}_1 \times \mathbf{T}_2|}, \quad (5)$$

where $\mathbf{T}_1 = (x_3 - x_1, y_3 - y_1, z_3 - z_1)$ and $\mathbf{T}_2 = (x_4 - x_1, y_4 - y_1, z_4 - z_1)$.

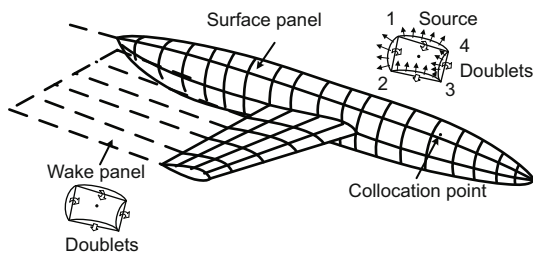


Fig. 5 Panel definition

2. The collocation point

$$\begin{cases} \bar{x} = \frac{1}{4} \sum_{k=1}^4 x_k, \\ \bar{y} = \frac{1}{4} \sum_{k=1}^4 y_k, \\ \bar{z} = \frac{1}{4} \sum_{k=1}^4 z_k. \end{cases} \quad (6)$$

3. Panel corner point

$$\begin{cases} x'_i = x_i + \mathbf{n}_x \cdot \mathbf{d}, \\ y'_i = y_i + \mathbf{n}_y \cdot \mathbf{d}, \\ z'_i = z_i + \mathbf{n}_z \cdot \mathbf{d}, \end{cases} \quad (7)$$

where $\mathbf{d} = \mathbf{n}_x(\bar{x} - x_i) + \mathbf{n}_y(\bar{y} - y_i) + \mathbf{n}_z(\bar{z} - z_i)$.

4. Panel length

$$d_{ij} = \sqrt{(x'_i - x'_j)^2 + (y'_i - y'_j)^2 + (z'_i - z'_j)^2}. \quad (8)$$

5. Panel area

$$\Delta S = \frac{\sqrt{\mathbf{T}_1 \times \mathbf{T}_2}}{2}. \quad (9)$$

2.2.2 Low-speed aerodynamics

Following Green's identity (Cummings et al., 2015), the potential perturbation at point P can be constructed by the sum of source σ and doublet μ singularities placed on the surface boundary:

$$\begin{aligned} \Delta\phi(P) = & \frac{1}{4\pi} \int_{S_B} \left[\mu \frac{\partial}{\partial(\mathbf{n})} \left(\frac{1}{r} \right) - \sigma \left(\frac{1}{r} \right) \right] dS \\ & + \frac{1}{4\pi} \int_{S_W} \left[\mu \frac{\partial}{\partial(\mathbf{n})} \left(\frac{1}{r} \right) \right] dS, \end{aligned} \quad (10)$$

where S_B refers to the body surface, S_W refers to the wake surface, and \mathbf{r} is the radius vector of point P .

With the vehicle surface being divided into N surface panels and N_w additional wake panels (Fig. 5), the Dirichlet boundary condition for each of the collocation points on the surface can be transformed into the discretized form:

$$\begin{aligned} \sum_{k=1}^N \frac{1}{4\pi} \int_{BP} \left[\mu \mathbf{n} \cdot \nabla \left(\frac{1}{r} \right) - \sigma \left(\frac{1}{r} \right) \right] dS \\ + \sum_{o=1}^{N_w} \frac{1}{4\pi} \int_{WP} \mu \mathbf{n} \cdot \nabla \left(\frac{1}{r} \right) dS = 0, \end{aligned} \quad (11)$$

where BP refers to the body panel and WP the wake panel.

For each collocation point, the summation of k body panels and o wake panels with constant singularity strength can be calculated numerically (Katz and Plotkin, 2001), and thus a linear algebraic equation set containing N unknown singularity variables μ_k can be derived

$$[A_{ij}][\mu_i] = -[b_{ij}][\sigma_i], \quad (12)$$

where A_{ij} is the doublet influence coefficient and b_{ij} the source influence coefficient.

Eq. (12) can be solved for the doublet strength with $\sigma_i = \mathbf{n}_i \cdot \mathbf{V}_\infty$, and hence the total flow velocity in the local panel coordinate is

$$\mathbf{V}_k = (V_{\infty l}, V_{\infty m}, V_{\infty n})_k + \left(-\frac{\partial \mu}{\partial l}, -\frac{\partial \mu}{\partial m}, -\sigma \right)_k, \quad (13)$$

where (l, m, n) is the unit orthogonal vector in the panel coordinate system.

The pressure coefficient can now be computed based on Bernoulli's equation:

$$C_{pk} = 1 - \frac{|\mathbf{V}_k|^2}{|\mathbf{V}_\infty|^2}. \quad (14)$$

2.2.3 Parasite drag

Only the lift-induced drag portion is provided by the potential flow theory introduced above, and an additional estimation of the viscous drag is required.

In this study, the skin friction and form drag contribution are estimated based on a built-up method, which calculates the parasite drag for each component and then sums to obtain the total parasite drag.

$$C_{D0} = \sum_{i=1}^K \frac{FF_i \cdot Q \cdot C_{Fi} \cdot S_{weti}}{S_{ref}}, \quad (15)$$

where K is the number of components, FF_i is the form factor of each component, S_{weti} is the component wetted area, Q is the interference factor,

and C_{Fi} is the skin-friction coefficient which is approximated using the Eckert reference temperature method (Lobbia, 2017) for laminar flow and the van Driest II formula for turbulent flow (Gur et al., 2010).

Form factors are calculated based on an empirical formula (Raymer, 2018).

1. Fuselage class

$$FF = 1.0 + 1.5 \left(\frac{d}{l} \right)^{1.5} + 7 \left(\frac{d}{l} \right)^3, \quad (16)$$

where d/l is the ratio of diameter to length.

2. Wing class

$$FF = 1.0 + 2.7 \left(\frac{t}{c} \right) + 100 \left(\frac{t}{c} \right)^4, \quad (17)$$

where t/c is the thickness ratio of a particular component.

2.3 Propulsion module

The mixed-flow turbofan engine with afterburner is used as the low-speed propulsion system, with the notation and station numbering (Fig. 6) in accordance with aerospace recommended practice (ARP) (Mattingly, 1996), which are listed in Table 1.

According to the momentum theorem, the uninstalled engine thrust can be written as

$$T = \dot{m}_9 V_9 - \dot{m}_0 V_0 + P_9 A_9 - P_0 A_0, \quad (18)$$

where station 0 is the free stream flow and station 9 is the engine exit, and \dot{m}_* represents the mass flow rate.

The problem setup and performance calculation steps of a dual-spool turbojet differ in on-design and off-design conditions. To calculate the off-design performance, an on-design mathematical model is first developed based on known design parameters.

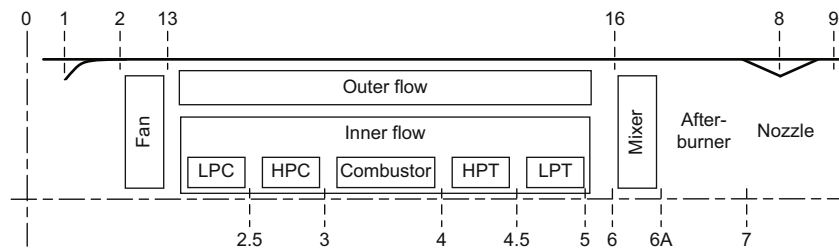


Fig. 6 Reference stations of mixed-flow turbofan engine with after-burner

Table 1 Subscript definition of different components

Subscript	Component	Station
AB	After-burner	6A-7
b	Burner	3-4
f	Fan	2-13
cH	High-pressure compressor	2-2.5
cL	Low-pressure compressor	2.5-3
d	Diffuser	0-2
M	Mixer	6-6A
n	Nozzle	7-9
tH	High-pressure turbine	4-4.5
tL	Low-pressure turbine	4.5-5

2.3.1 On-design performance analysis

Eq. (18) can be rewritten in terms of total pressure and total temperature ratios as follows:

$$\frac{F}{\dot{m}_0 V_0} = (1 + f + f_{AB}) \frac{V_9}{V_0} - M_0 + (1 + f + f_{AB}) \frac{R_{AB}}{R_c} \frac{T_9/T_0}{V_9/V_0} \frac{1 - P_0/P_9}{\gamma_c}, \quad (19)$$

where subscript “c” refers to the free-stream condition, f_* is the fuel/air ratio, T_* is the static temperature, R_* is the gas constant, M_* is the Mach number in the engine flowpath, and γ_c is the specific heat ratio.

Application of the first law of thermodynamics to the main combustor gives

$$\dot{m}_0 c_{pc} T_{t3} + \eta_b \dot{m}_f h_{PR} = \dot{m}_4 c_{pt} T_{t4}, \quad (20)$$

where c_{p*} is the specific heat, h_{PR} is the lower heating value of the fuel, T_{t*} is the total temperature, and η_b is the burner efficiency. By solving this equation, we can obtain the fuel/air ratio of main-burner, i.e.

$$f = \frac{\tau_\lambda - \tau_r \tau_{cH} \tau_{cL}}{\eta_b h_{PR} / (c_{pc} T_0) - \tau_\lambda}, \quad (21)$$

where τ_* is the total temperature ratio.

A similar process is applied to the after-burner:

$$f_{AB} = (1 + f) \frac{\tau_{\lambda AB} - \tau_\lambda \tau_{tH} \tau_{tL} \tau_M}{\eta_{AB} h_{PR} / (c_{pc} T_0) - \tau_{\lambda AB}}. \quad (22)$$

The power balance of each spool is given by

$$\begin{cases} \eta_{mH} \dot{m}_4 c_{pt} (T_{t4} - T_{t4.5}) = \dot{m}_2 c_{pc} (T_{t3} - T_{t2.5}), \\ \eta_{mL} \dot{m}_{4.5} c_{pt} (T_{t4.5} - T_{t5}) = \dot{m}_2 c_{pc} (T_{t2.5} - T_{t2}), \end{cases} \quad (23)$$

which allows the calculation of the total temperature ratio:

$$\begin{cases} \tau_{tH} = 1 - \frac{\tau_r \tau_{cL} (\tau_{cH} - 1)}{\eta_{mH} \tau_\lambda (1 + f)}, \\ \tau_{tL} = 1 - \frac{\tau_r [(\tau_{cL} - 1) + \alpha_f (\tau_f - 1)]}{\eta_{mL} \tau_\lambda \tau_{tH}}, \end{cases} \quad (24)$$

where η_{m*} is the turbine shaft power transmission efficiency and α_f is the bypass ratio.

With all these component's performance variables available, the overall engine thrust can be calculated with Eq. (18).

2.3.2 Off-design performance analysis

The off-design performance analysis can be evaluated with the steady-state operating point assumption (Mattingly et al., 2002), that is,

$$f(\tau, \pi) = f(\tau_R, \pi_R) = \text{constant}, \quad (25)$$

where $f(\cdot)$ represents the functional relations for engine cycle analysis, which are based on the application of mass, energy, momentum, and entropy considerations, and the subscript R represents the on-design condition.

The solutions of the dependent variables between stations 2 and 6A are calculated based on the following flowchart (Fig. 7), where initial values are selected to be equal to their on-design reference values.

3 Stability and control analysis

To characterize vehicle controllability, stability and control analysis is conducted, aiming to obtain the CG limits. For air-breathing HTHL aerospace vehicles, the forward and aft CG limits are computed considering the following main factors: (1) static stability; (2) take-off rotation; (3) landing nose hold-off. Other dynamic stability analysis modules can also be added.

3.1 Static stability constraint

Static stability is considered to be a good indicator of a vehicle's overall stability, and it describes the initial tendency in a trimmed condition to return to that equilibrium under perturbation. Too statically stable vehicles will feel sluggish and less maneuverable, while marginally stable ones will be very

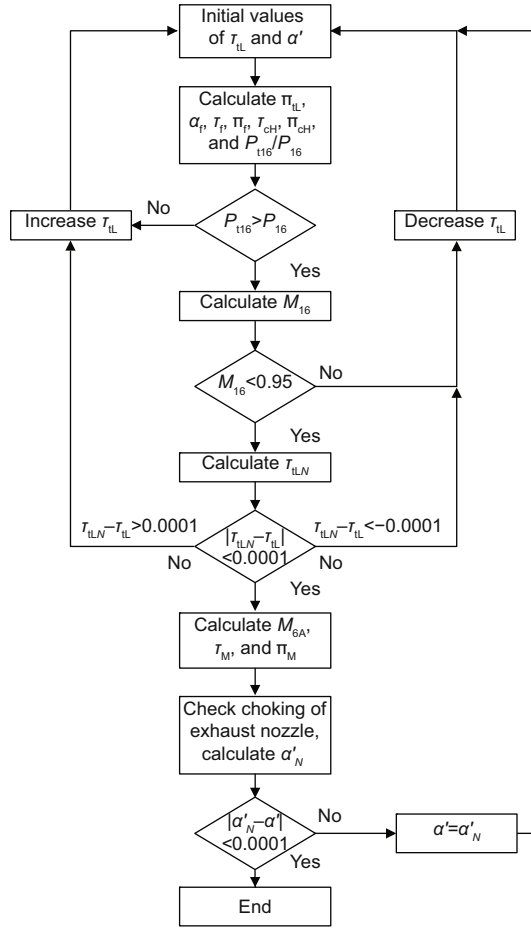


Fig. 7 Flowchart of mixed-flow turbfan performance analysis (α' refers to the mixer bypass ratio and subscript N refers to the iteration variable)

sensitive to external disturbances. In addition, the static stability of the aerospace vehicle has a serious impact on trim drag and the control power required. Thus, it is often desirable to set the center of gravity at the point which requires little effort to maintain trim condition.

3.2 Take-off rotation maneuver constraint

We assume that the air-breathing aerospace vehicle concept is equipped with a tricycle-gear system. For rotation analysis (Fig. 8), the nose gear is just resting on the runway without carrying any weight ($N_f = 0$) and the engine installation angle is ignored. Then force and moment equations of the vehicle can be written as

$$\begin{cases} G - L_a - N_b - T \sin \alpha_0 = 0, \\ -N_b X_b - f_b Z_f + T Z_T + M_R = 0, \end{cases} \quad (26)$$

where G is the force of gravity, L_a is the lift, N_b is the main gear load, f_b is the main gear rolling friction, T is the thrust, α_0 is the vehicle ground angle, M_R is the aerodynamic pitching moment, and X_b , Z_T , and Z_f are corresponding moment arms.

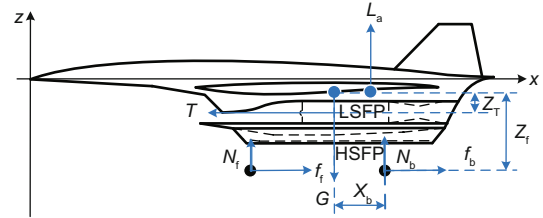


Fig. 8 Major forces and moment arm definition during rotation (N_f : nose gear load; f_f : nose gear rolling friction)

As the vehicle reaches force balance in the longitudinal direction, the shock strut force of the main gear can be obtained as follows:

$$N_b = G - L_a - T \sin \alpha_0. \quad (27)$$

Assuming $\alpha_0 = 0$ and substituting Eq. (27) into Eq. (26), we have

$$M_{\text{total}} = M_R + T Z_T - (G - L_a) X_b - \mu_0 (G - L_a) Z_f, \quad (28)$$

where μ_0 is the rolling friction coefficient and M_{total} is the total pitching moment acting on the vehicle.

To successfully achieve a take-off rotation maneuver, the necessary condition $M_{\text{total}} \geq 0$ should be satisfied.

3.3 Landing nose hold-off constraint

The landing nose hold-off trim condition ensures that the nose gear will not crash into the runway during touch-down. The analysis is similar to that of the take-off rotation maneuver, using the same equations (Eq. (26)), but with the weight at the end of the descent and no thrust.

4 Simulation results

4.1 Concept description

As shown in Fig. 9, the proposed air-breathing HTHL aerospace vehicle features a compact blended wing-body configuration, equipped with a strake, a trapezoid wing, and a tail. The over-under TBCC module is housed in an engine nacelle underslung to

the midsection of the fuselage, with the forebody undersurface acting as an external inlet, and the aft body undersurface acting as an external nozzle, resulting in an airframe integrated propulsion system. The main characteristic parameters of this vehicle are listed in Table 2 for convenience.

4.2 Aerodynamic surrogate model

The aerodynamic database of the low-speed envelope (Table 3) is generated based on the above-mentioned methods.

All of the aerodynamic coefficients are presented in two separate parts: clean configuration $C_{i(\text{clean})}$ and incremental addition due to control surface deflections $\Delta C_{i(\delta_e)}$.

Each term can be interpolated for a given flight condition and control input and then combined to obtain the aerodynamic coefficient of interest.

$$\begin{aligned} C_{i(\text{total})} &= C_{i(\text{clean})} + \Delta C_{i(\delta_e)} \\ &= C_{i(\text{clean})} + C_i^{\delta_e} \delta_e. \end{aligned} \quad (29)$$

The results, the truth model (TM), can be calibrated with the supposedly known aerodynamic coefficients of the initial design. To render these coefficients more tractable, regression analysis is performed and the appropriate control-oriented polynomial models (COMs) of the longitudinal aerodynamic coefficients are given (i.e. C_i , $i \in \{L, D, m\}$).

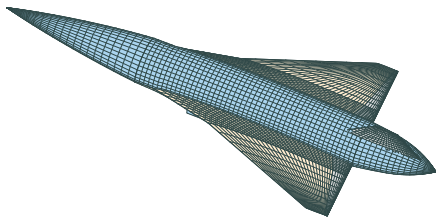


Fig. 9 Mesh view of the concept vehicle

Table 2 Main geometric characteristics of the concept vehicle

L (m)	H (m)	S_{ref} (m ²)	c_{ref} (m)	b (m)
28	7	103.3	10.16	10.66

c_{ref} : mean aerodynamic chord; b : span

Table 3 Low-speed state summary

State	Range		State	Range
Ma	[0, 0.9]		α (°)	[-6, 15]
H (km)	[0, 20]		δ_e (°)	[-20, 20]

Ma : Mach number; H : altitude; α : angle of attack; δ_e : elevon

4.2.1 Clean configuration coefficients

It is well-known that the lift coefficient of the clean vehicle consists of two terms, as follows:

$$C_L = C_{L0} + C_{L\alpha}\alpha, \quad (30)$$

where α is the angle of attack.

Considering Mach number effects, stepwise regression (SWR) analysis is adopted, and the resulting COM structures are shown below:

$$\begin{aligned} C_{L(\text{clean})} &= C_{L0} + C_{L\alpha}\alpha \\ &= (a_0 + a_1 Ma) + (a_2 + a_3 Ma)\alpha. \end{aligned} \quad (31)$$

The drag coefficients can be described with the conventional form of the lift-drag polar equation:

$$\begin{aligned} C_{D(\text{clean})} &= C_{D0} + k C_{L(\text{clean})}^2 \\ &= (b_0 + b_1 Ma) + (b_2 + b_3 Ma) C_{L(\text{clean})}^2. \end{aligned} \quad (32)$$

A similar process is applied to compute the pitching moment coefficients of the clean vehicle:

$$\begin{aligned} C_{m(\text{clean})} &= C_{m0} + C_{m\alpha}\alpha \\ &= (c_0 + c_1 Ma) + (c_2 + c_3 Ma)\alpha. \end{aligned} \quad (33)$$

As can be seen in Fig. 10, all these resulting SWR models (colored surface) satisfactorily approximate TM data ("*" in the figure), and can be used as the control-oriented surrogate model.

4.2.2 Incremental coefficients

The control effectiveness computation of the elevon with a discretized chord is described in this subsection. The surrogate modeling is performed only with the initial elevon layout. The variable geometry surrogate modeling process can also be conducted in the same way, wherein configurations with discretized chord are analyzed and fitted with the same expression form, leaving the coefficient modifications to a higher tier of the framework.

The final formulae with satisfactory fitting accuracy are confirmed as follows:

$$\begin{cases} C_L^{\delta_e} = a_4 + a_5 Ma + a_6 \alpha, \\ C_D^{\delta_e} = b_5 + b_6 \delta_e + b_7 Ma + b_8 \alpha + b_9 (Ma)^2 \delta_e, \\ C_m^{\delta_e} = c_4 + c_5 \alpha^2 + c_6 Ma + c_7 (Ma)^2. \end{cases} \quad (34)$$

The corresponding results of $\delta_e = -20^\circ, -10^\circ, 0^\circ, 10^\circ$, and 20° are presented in Fig. 11, indicating that these results agree very well with the high fidelity model.

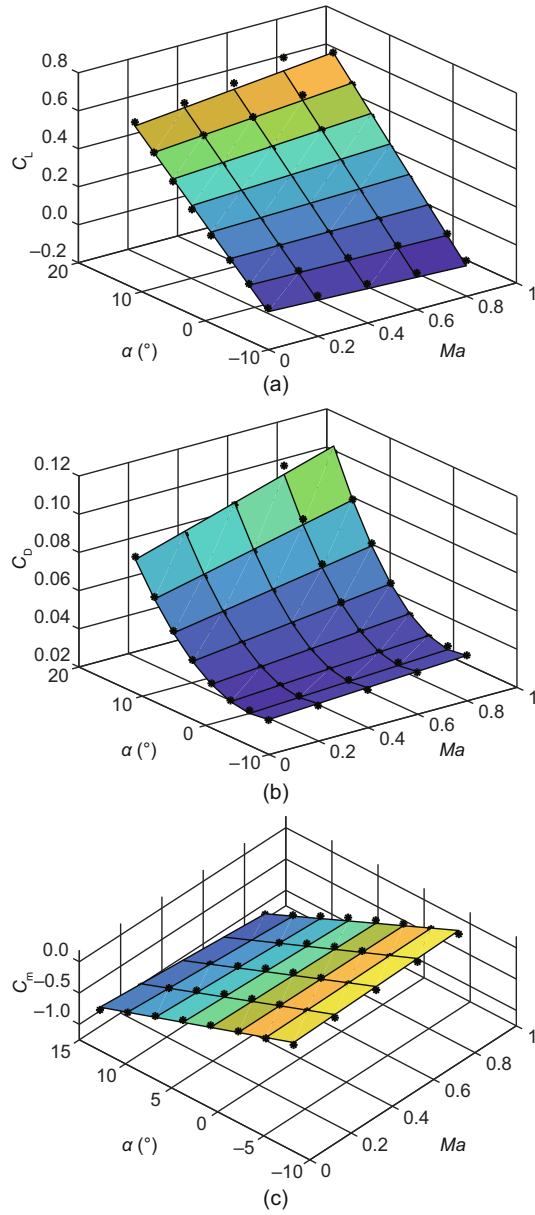


Fig. 10 Clean configuration aerodynamic coefficients: (a) C_L ; (b) C_D ; (c) C_m . References to color refer to the online version of this article

Goodness of fit (GOF) and root mean square error (RMSE) are selected as the quantitative assessment metrics, and the results in Table 4 demonstrate that the control-oriented polynomial model has high accuracy and is suitable for the following system analysis.

4.3 Propulsion surrogate model

During engine performance analysis, various combinations of altitude and Mach number can be

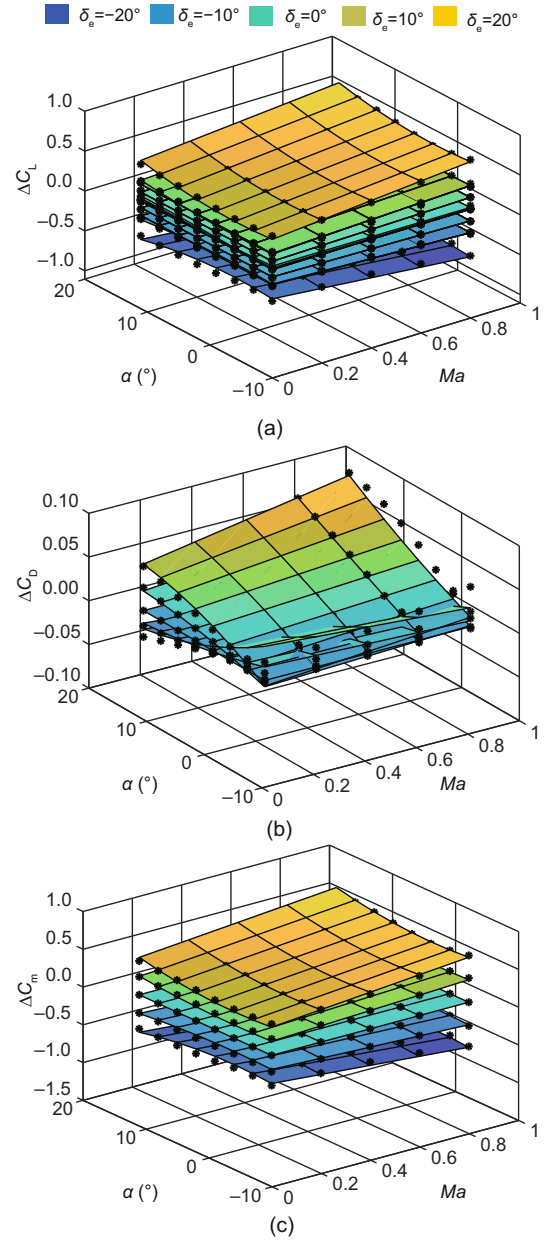


Fig. 11 Incremental aerodynamic coefficients ($\eta = 20\%$): (a) ΔC_L ; (b) ΔC_D ; (c) ΔC_m . References to color refer to the online version of this article

represented by a specific value of θ_0 :

$$\theta_0 = T_t/T_{SLS} = T/T_{SLS} \left(1 + \frac{\gamma_c - 1}{2} (Ma)^2 \right). \quad (35)$$

The installed thrust is given by

$$T = \phi \alpha_t (Ma, H) T_{SLS} = \phi \alpha_t (\theta_0) T_{SLS} (TR), \quad (36)$$

where ϕ is the non-dimensional ratio of output thrust to the maximum available thrust, α_t is the installed full throttle thrust lapse which depends on speed

Table 4 Validation results of surrogate models ($\eta = 20\%$)

Variable	GOF	RMSE	Variable	GOF	RMSE
C_m	0.9871	0.0431	ΔC_m	0.9824	0.0495
C_L	0.9915	0.0213	ΔC_L	0.9809	0.0253
C_D	0.9881	0.0027	ΔC_D	0.9679	0.0045

GOF: goodness of fit; RMSE: root mean square error

(Ma) and altitude (H), and can be defined as functions of non-dimensional temperature θ_0 . TR is the throttle ratio, which equals $\theta_{0\text{break}}$:

$$\text{TR} = \frac{T_{t4\text{max}}}{T_{t4\text{SLS}}} = \theta_{0\text{break}}, \quad (37)$$

where $T_{t4\text{max}}$ is the maximum allowable combustor exit temperature and $T_{t4\text{SLS}}$ is the air temperature at sea-level static condition.

Control systems must be designed to protect the engine from exceeding some operational constraints. The most significant ones are the maximum allowable values of π_c and T_{t4} .

For flight conditions where $\theta_0 < \text{TR}$, the engine is π_c -limited and the ratio of T_{t4}/θ_0 remains constant. For flight conditions where $\theta_0 > \text{TR}$, the engine is T_{t4} -limited, and thus the maximum value of T_{t4} is $T_{t4\text{max}}$.

With the above control logic taken into account, the available thrust can be written into piecewise polynomials about the throttle ratio (Mattingly et al., 2002):

$$\alpha_t = \begin{cases} \delta_0, & \theta_0 \leq \text{TR}, \\ \delta_0 [1 - 3.5(\theta_0 - \text{TR})/\theta_0], & \theta_0 > \text{TR}, \end{cases} \quad (38)$$

where δ_0 is the non-dimensional pressure ratio:

$$\delta_0 = P_t/P_{\text{SLS}} = P/P_{\text{SLS}} \left(1 + \frac{\gamma_c - 1}{2} M_0^2 \right)^{\gamma_c/(\gamma_c - 1)}. \quad (39)$$

4.4 Center-of-gravity trade-off analysis

The moment coefficients in the database are calculated around the reference point (R), which does not coincide with the CG. To better understand the aircraft rotational motion, the moment coefficients obtained from the pre-flight aerodynamic database are transformed about the CG by Eq. (40) (no sideslip considered):

$$\begin{aligned} C_{mC} = & C_{mR} + (x_R - x_C)(C_D \sin \alpha + C_L \cos \alpha)/c \\ & + (z_R - z_C)(-C_D \cos \alpha + C_L \sin \alpha)/c. \end{aligned} \quad (40)$$

A non-dimensional coefficient, representing the CG position along the longitudinal axis in percent fuselage length is defined as \bar{x}_{CG} :

$$\bar{x}_{CG} = x_{CG}/L. \quad (41)$$

The goal of the present S&C analysis is to act as a feasibility test for air-breathing aerospace vehicles, thus to find a suitable CG position \bar{x}_{CG} , satisfying all the constraints in Section 3.

4.4.1 Static stability constraint

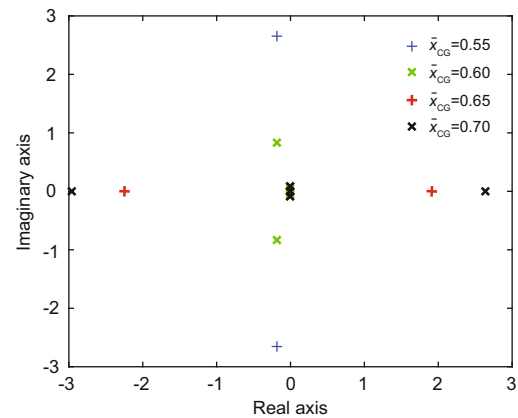
A typical operation point for the aerospace vehicle is selected to be (Ma 0.6, 8 km) during the subsonic cruise and loiter phase.

The vehicle is trimmed for discretized CG positions. As \bar{x}_{CG} moves aft from 0.55 to 0.70, the short-period eigenvalues are typically oscillatory at first, and then degenerate into overdamped real roots that diverge from each other along the real axis. Eventually, one of the short-period roots crosses the imaginary axis and the aerospace vehicle becomes longitudinally unstable (Fig. 12).

To minimize the trim drag, the allowable CG travel range is selected to be $\bar{x}_{CG} \in [0.60, 0.65]$, which corresponds to $\delta_e \in [-5^\circ, 5^\circ]$ (Fig. 13).

4.4.2 Take-off rotation maneuver constraint

Assuming that the mixed-flow turbofan engine is at the maximum power condition, the total pitching moment acting on the vehicle with different CG positions is shown in Fig. 14. Only the aft limit of the CG position $\bar{x}_{CG} = 0.65$ meets the conditions that $M_{\text{total}} \geq 0$, which satisfies the take-off rotation constraint.

**Fig. 12** Open-loop eigenvalues of the longitudinal model

4.4.3 Landing nose hold-off constraint

Neglecting the thrust contribution, the total pitching moment acting on the vehicle during the landing phase is presented in Fig. 15. Only the aft limit of the CG position $\bar{x}_{CG} = 0.65$ meets the conditions that $M_{total} \geq 0$, indicating that the vehicle

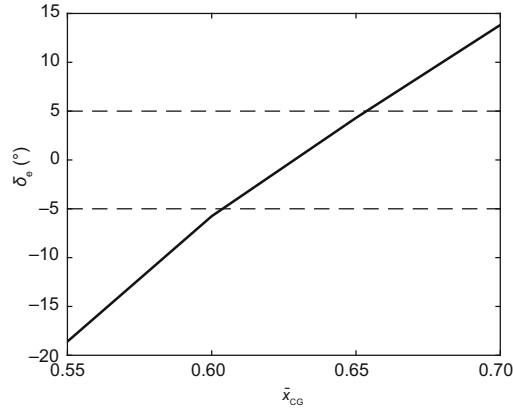


Fig. 13 Trim elevon deflections with different CG positions

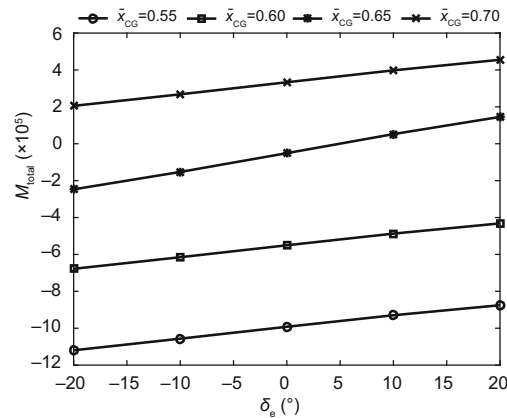


Fig. 14 M_{total} for different elevon deflections (take-off)

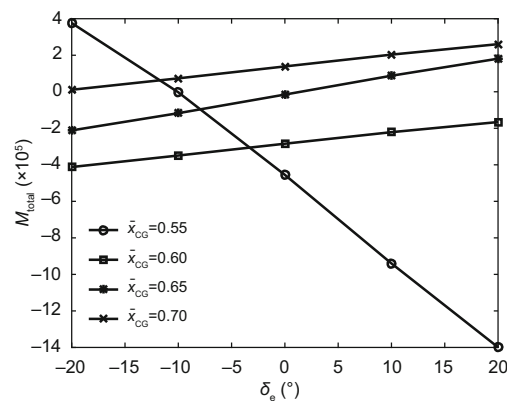


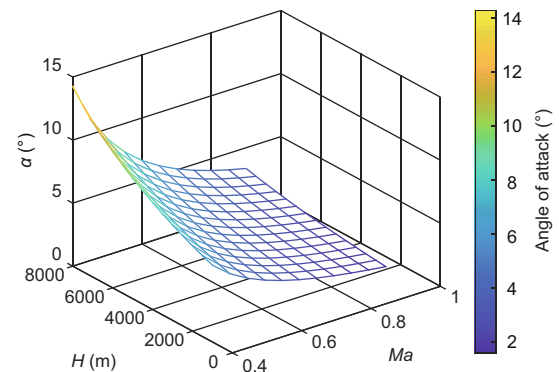
Fig. 15 M_{total} for different elevon deflections (landing)

can land horizontally successfully.

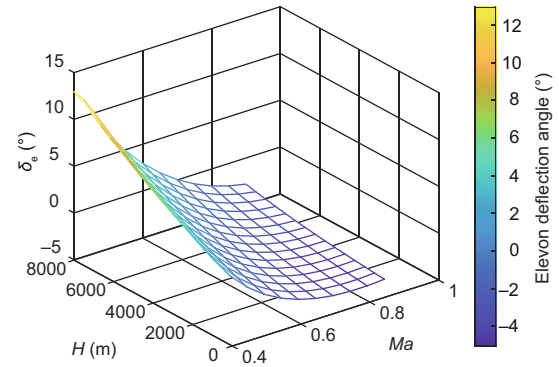
4.4.4 Trim region analysis

With the CG position fixed at $\bar{x}_{CG} = 0.65$, the proposed vehicle concept has a negative static margin. Pitch trim is accomplished using only the elevon, and the corresponding control variables are shown in Fig. 16.

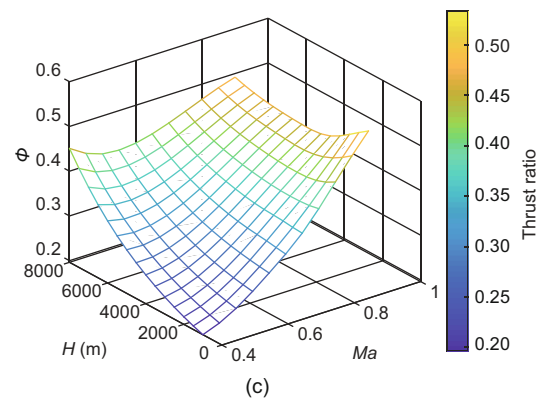
It is clearly indicated that the elevon's deflection angle is less than the maximum allowable of 20° and the non-dimensional thrust ratio is less than



(a)



(b)



(c)

Fig. 16 Trim states as function of altitude and Mach number ($\bar{x}_{CG} = 65\%$): (a) α ; (b) δ_e ; (c) ϕ

one, demonstrating the utility of the proposed vehicle concept.

5 Conclusions

We have presented a control-oriented low-speed dynamic model for conceptual TBCC engine powered aerospace vehicle, which can realize HTHL like a normal plane. The framework consists of mainly four modules: (1) parametric geometry modeling; (2) potential theory based panel method; (3) quasi-1D mixed-flow turbofan model; (4) regression analysis and surrogate modeling. A conceptual aerospace vehicle has been introduced based on the above-mentioned modeling framework. Stability and control analysis then has been conducted, with emphasis on take-off rotation and trim capabilities. Simulation results indicated that the proposed framework is appropriate for conceptual aerospace vehicle design, and it is essential to conduct integrated S&C analysis in the early design process of HTHL aerospace vehicles.

Contributors

Hai-dong SHEN and Yu-ping LU designed the research. Rui CAO and Fei-teng JIN processed the corresponding data. Hai-dong SHEN and Yan-bin LIU wrote the draft of the manuscript. Yu-ping LU helped organize the manuscript. Hai-dong SHEN and Yan-bin LIU revised and edited the final version. Hai-dong SHEN, Yan-bin LIU, and Yu-ping LU provided funding acquisitions.

Conflict of interest

Hai-dong SHEN, Rui CAO, Yan-bin LIU, Fei-teng JIN, and Yu-ping LU declare that they have no conflict of interest.

References

- Anderson JD, 2010. Fundamentals of Aerodynamics. McGraw-Hill, New York, USA.
- Bowcutt K, 2003. A perspective on the future of aerospace vehicle design. Proceedings of the 12th AIAA International Space Planes and Hypersonic Systems and Technologies, Article 6957.
<https://doi.org/10.2514/6.2003-6957>
- Bradford JE, Charanja A, Wallace J, et al., 2004. Quicksat: a two stage to orbit reusable launch vehicle utilizing air breathing propulsion for responsive space access. Proceedings of Space 2004 Conference and Exhibit, Article 5950.
<https://doi.org/10.2514/6.2004-5950>
- Chen BY, Liu YB, Shen HD, et al., 2017. Surrogate modeling of a 3D scramjet-powered hypersonic vehicle based on screening method IFFD. *Proceedings of the Institution of Mechanical Engineers, Part G: Journal of Aerospace Engineering*, 231(2):265-278.
<https://doi.org/10.1177/0954410016636161>
- Cummings RM, Mason WH, Morton SA, et al., 2015. Applied Computational Aerodynamics: a Modern Engineering Approach. Cambridge University Press, New York, USA.
- Erickson LL, 1990. Panel Methods: an Introduction. NASA-TP-2995, NASA, Washington, USA.
- Fernández-Villacé V, Paniagua G, Steelant J, 2014. Installed performance evaluation of an air turbo-rocket expander engine. *Aerospace Science and Technology*, 35:63-79.
<https://doi.org/10.1016/j.ast.2014.03.005>
- Gur O, Mason WH, Schetz JA, 2010. Full-configuration drag estimation. *Journal of Aircraft*, 47(4):1356-1367.
<https://doi.org/10.2514/1.47557>
- Hellman BM, Bradford J, St. Germain B, et al., 2016. Two stage to orbit conceptual vehicle designs using the SABRE engine. Proceedings of AIAA SPACE, Article 5320.
<https://doi.org/10.2514/6.2016-5320>
- Jazra T, Smart M, 2009. Development of an aerodynamics code for the optimisation of hypersonic vehicles. Proceedings of the 47th AIAA Aerospace Sciences Meeting Including the New Horizons Forum and Aerospace Exposition, Article 1475.
<https://doi.org/10.2514/6.2009-1475>
- Katz J, Plotkin A, 2001. Low-speed Aerodynamics (2nd Edition). Cambridge University Press, Cambridge, UK.
- Kokan T, Olds JR, Hutchinson V, et al., 2004. Aztec: a TSTO hypersonic vehicle concept utilizing TBCC and HEDM propulsion technologies. Proceedings of the 40th AIAA/ASME/SAE/ASEE Joint Propulsion Conference and Exhibit, Article 3728.
<https://doi.org/10.2514/6.2004-3728>
- Kulfan BM, 2008. Universal parametric geometry representation method. *Journal of Aircraft*, 45(1):142-158.
<https://doi.org/10.2514/1.29958>
- Liao L, Yan L, Huang W, et al., 2018. Mode transition process in a typical strut-based scramjet combustor based on a parametric study. *Journal of Zhejiang University-SCIENCE A (Applied Physics & Engineering)*, 19(6):431-451.
<https://doi.org/10.1631/jzus.A1700617>
- Liu CZ, Duan YH, Cai JS, et al., 2016. Application of the 3D multi-block CST method to hypersonic aircraft optimization. *Aerospace Science and Technology*, 50:295-303.
<https://doi.org/10.1016/j.ast.2015.06.019>
- Lobbia MA, 2017. Rapid supersonic/hypersonic aerodynamics analysis model for arbitrary geometries. *Journal of Spacecraft and Rockets*, 54(1):315-322.
<https://doi.org/10.2514/1.A33514>

- Longo JMA, Dittrich R, Banuti D, et al., 2009. Concept study for a Mach 6 transport aircraft. Proceedings of the 47th AIAA Aerospace Sciences Meeting Including the New Horizons Forum and Aerospace Exposition, Article 435.
<https://doi.org/10.2514/6.2009-435>
- Ma JX, Chang JT, Ma JC, et al., 2018. Mathematical modeling and characteristic analysis for over-under turbine based combined cycle engine. *Acta Astronautica*, 148:141-152.
<https://doi.org/10.1016/j.actaastro.2018.04.050>
- Mattingly JD, 1996. Elements of Gas Turbine Propulsion. McGraw-Hill, New Delhi, India.
- Mattingly JD, Heiser WH, Pratt DT, 2002. Aircraft Engine Design. American Institute of Aeronautics and Astronautics, Reston, USA.
- McDaniel JC, Chelliah H, Goynes C, et al., 2009. US national center for hypersonic combined cycle propulsion: an overview. Proceedings of the 16th AIAA/DLR/DGLR International Space Planes and Hypersonic Systems and Technologies Conference, Article 7280.
<https://doi.org/10.2514/6.2009-7280>
- Mehta U, Aftosmis M, Bowles J, et al., 2016. Sky-lon aerospace plane and its aerodynamics and plumes. *Journal of Spacecraft and Rockets*, 53(2):340-353.
<https://doi.org/10.2514/1.A33408>
- Moses PL, Bouchard KA, Vause RF, et al., 1999. An air-breathing launch vehicle design with turbine-based low-speed propulsion and dual mode scramjet high-speed propulsion. Proceedings of the 9th International Space Planes and Hypersonic Systems and Technologies Conference, Article 4948.
<https://doi.org/10.2514/6.1999-4948>
- Piscitelli F, Cutrone L, Pezzella G, et al., 2017. Nose-to-tail analysis of an airbreathing hypersonic vehicle using an in-house simplified tool. *Acta Astronautica*, 136:148-158.
<https://doi.org/10.1016/j.actaastro.2017.03.007>
- Raymer DP, 2018. Aircraft Design: a Conceptual Approach (6th Edition). American Institute of Aeronautics and Astronautics, Reston, USA.
<https://doi.org/10.2514/4.104909>
- Roncioni P, Natale P, Marini M, et al., 2015. Numerical simulations and performance assessment of a scramjet powered cruise vehicle at Mach 8. *Aerospace Science and Technology*, 42:218-228.
<https://doi.org/10.1016/j.ast.2015.01.006>
- Shen HD, Liu YB, Chen BY, et al., 2018. Control-relevant modeling and performance limitation analysis for flexible air-breathing hypersonic vehicles. *Aerospace Science and Technology*, 76:340-349.
<https://doi.org/10.1016/j.ast.2018.02.016>
- Spoth KA, Moses PL, 1993. Structural design and analysis of a Mach zero to five turbo-ramjet system. Proceedings of the 29th Joint Propulsion Conference and Exhibit, Article 1983.
<https://doi.org/10.2514/6.1993-1983>
- Stueber TJ, Vrnak DR, Le DK, et al., 2010. Control Activity in Support of NASA Turbine Based Combined Cycle (TBCC) Research. NASA/TM-2010-216109, E-17192, NASA, CA, USA.
- Sziroczak D, Smith H, 2016. A review of design issues specific to hypersonic flight vehicles. *Progress in Aerospace Sciences*, 84:1-28.
<https://doi.org/10.1016/j.paerosci.2016.04.001>
- Tsuchiya T, Mori T, 2005. Optimal design of two-stage-to-orbit space planes with airbreathing engines. *Journal of Spacecraft and Rockets*, 42(1):90-97.
<https://doi.org/10.2514/1.8012>
- Walker S, Tang M, Mamplata C, 2009. TBCC propulsion for a Mach 6 hypersonic airplane. Proceedings of the 16th AIAA/DLR/DGLR International Space Planes and Hypersonic Systems and Technologies Conference, Article 7238.
<https://doi.org/10.2514/6.2009-7238>
- Zhang TT, Wang ZG, Huang W, et al., 2016a. Parameterization and optimization of hypersonic-gliding vehicle configurations during conceptual design. *Aerospace Science and Technology*, 58:225-234.
<https://doi.org/10.1016/j.ast.2016.08.020>
- Zhang TT, Huang W, Wang ZG, et al., 2016b. A study of airfoil parameterization, modeling, and optimization based on the computational fluid dynamics method. *Journal of Zhejiang University-SCIENCE A (Applied Physics & Engineering)*, 17(8):632-645.
<https://doi.org/10.1631/jzus.A1500308>
- Zhang TT, Wang ZG, Huang W, et al., 2018. A review of parametric approaches specific to aerodynamic design process. *Acta Astronautica*, 145:319-331.
<https://doi.org/10.1016/j.actaastro.2018.02.011>
- Zhang TT, Wang ZG, Huang W, et al., 2019. The overall layout of rocket-based combined-cycle engines: a review. *Journal of Zhejiang University-SCIENCE A (Applied Physics & Engineering)*, 20(3):163-183.
<https://doi.org/10.1631/jzus.A1800684>
- Zhao ZT, Huang W, Yan L, et al., 2019. Low speed aerodynamic performance analysis of vortex lift waveriders with a wide-speed range. *Acta Astronautica*, 161:209-221.
<https://doi.org/10.1016/j.actaastro.2019.05.029>
- Zhou JX, Lu H, Zhang HC, et al., 2017. A preliminary research on a two-stage-to-orbit vehicle with airbreathing pre-cooled hypersonic engines. Proceedings of the 21st AIAA International Space Planes and Hypersonics Technologies Conference, Article 2343.
<https://doi.org/10.2514/6.2017-2343>

中文概要

题 目：面向控制的空天飞行器低速段动力学建模及性能折衷分析

目 的: 水平起降空天飞行器需兼顾高速巡航和低速起降性能。本文旨在构建一种面向控制的空天飞行器低速段动力学建模与迭代分析流程,探究质心位置对空天飞行器稳定性及控制性能的影响,并在保证空天飞行器水平起降能力的约束下,迭代获得合理的飞行器质心位置。

创新点: 1. 结合几何外形参数化方法、势流理论和0维混合排气涡扇发动机建模方法实现空天飞行器低速段气动/推进性能数据的快速获取; 2. 基于所获得的气动/推进性能数据,开展代理建模研究,获得适用于性能分析及控制器设计需要的气动力/力矩系数代理模型; 3. 基于可变质心的气动力/力矩系数代理模型进行空天飞行器水平起降性能分析及质心位置迭代设计。

方 法: 1. 通过形状/类型函数法建立空天飞行器几何参数化模型; 2. 基于势流理论和0维涡扇发动机理论快速获取空

天飞行器低速段气动/推进性能数据; 3. 通过代理模型技术,获得不同质心位置下的飞行器气动力/力矩系数拟合表达式,并基于该表达式确定符合水平起降约束的质心位置。

结 论: 1. 空天飞行器研究中,需综合考虑高低速性能,并协调水平起降、稳定性和控制性能等多方面指标; 2. 本文所提出的空天飞行器概念方案,满足抬头、触地约束的质心范围在距机头65%机身长度处; 3. 本文所提出的面向控制建模与性能分析流程可以满足空天飞行器概念方案阶段数据快速获取、方案快速迭代优化的要求。

关键词: 面向控制建模; 水平起降; 稳定性与控制分析; 性能折衷分析